Crystal structure, electrical properties and electronic band structure of tantalum ditelluride

1998 J. Phys.: Condens. Matter 10 761

(http://iopscience.iop.org/0953-8984/10/4/006)

J. Phys.: Condens. Matter **10** (1998) 761–774. Printed in the UK PII: S0953-8984(98)85989-4

Crystal structure, electrical properties and electronic band structure of tantalum ditelluride

A Vernes†§, H Ebert†, W Bensch‡, W Heid‡ and C Näther§

† Institut für Physikalische Chemie, Universität München, Theresienstrasse 37, D-80333 München, Germany

‡ Institut für Anorganische Chemie, Universität Kiel, Olshausenstrasse 40, D-24098 Kiel, Germany

Received 11 July 1997

Abstract. Motivated by the unexpectedly strong influence of the Te atoms on the structural and bonding properties of the transition metal tellurides, we have performed a detailed study of $TaTe_2$. Experimentally, this comprises a crystal structure determination as well as electrical resistivity measurements. The former analysis leads to an accurate update of the structural data reported in the 1960s, while the latter provides evidence for the mainly electronic character of scattering processes leading to the electrical conductivity. In addition, the electronic properties of $TaTe_2$ have been calculated using the TB-LMTO method. The partial density of states reflects the close connection of the Ta zigzag chains and the Te–Te network. This finding explains the charge transfer in the system in a rather simple way. The orthogonal-orbital character of the bands proved the existence of π-bonds. The Fermi-surface study supports the interpretation of the experimental resistivity measurements.

1. Introduction

The structural and bonding properties of transition metal tellurides have become an important field in recent solid-state research [1–6]. In a number of contributions it was demonstrated that tellurium behaves rather differently to the lighter homologues sulphur and selenium, and that the behaviour of Te may be classified as 'non-classical' as regards its bonding properties [7]. In addition, during the last few years the discoveries of a large number of new and exciting metal tellurides which demonstrate this 'non-classical' behaviour of tellurium [8–12] have been reported. In spite of this activity and the revival of inorganic solid-state tellurium chemistry, the crystal structures and physical properties of a large number of 'simple' transition metal tellurides are not exactly known. It is noteworthy that the structures of $PdTe_2$ [13] and Cr_5Te_8 [14], for example, were reported only very recently. To the best of our knowledge, the exact structures and properties of $HfTe_2$ and $ZrTe_2$, for instance, are still not known.

Motivated by the importance of tellurium compound chemistry and to achieve a better understanding of the bonding properties, we started to reinvestigate different transition metal tellurium systems [15, 16].

From a formal point of view, the Ta centres in $TaTe_2$ have a d^1 electronic configuration. As for many transition metal compounds with the metal centres exhibiting such an electron count [17–20], one would expect Ta–Ta bond formation with the typical pattern of alternating

§ To whom any correspondence should be addressed.

0953-8984/98/040761+14$19.50

short and long Ta–Ta distances. Contrary to this assumption, the Ta centres cluster to form double-zigzag chains, a behaviour observed for metal centres with a d^2 configuration. With the aim of achieving a better understanding of this unexpected behaviour, we decided to investigate $TaTe_2$ as regards the theoretical electronic band structure and the electrical properties. The crystal structure of $TaTe_2$ was first determined by Brown using the multiple Weissenberg method [21]. Because of the limited accuracy of this structure determination, we have redetermined the crystal structure to get more accurate data for our band-structure calculations.

2. Experimental details

As a first preparation step, the ternary telluride $NiTaTe_5$ was prepared according to the conditions given in [22]. The thermal decomposition of this compound at temperatures above the preparation temperature leads to the formation of $NiTe_2$, $TaTe_2$ and Te. The crystals of the ditellurides were of good quality, allowing single-crystal x-ray work and electrical characterization.

Table 1. Technical details of the single-crystal x-ray diffraction investigations for $TaTe_2$ and selected refinement results obtained at 295 K and 120 K. (x is the extinction correction: $F^* = F[1 + 0.002F^2/\sin(2\Theta)]^{-1/4}$; w provides the weighting scheme: $w^{-1} = \sigma^2(F) + yF^2$.)

T (K)	295	120
a (Å)	14.800(2)	14.761(3)
b (Å)	3.6424(5)	3.631(1)
c (Å)	9.347(1)	9.320(2)
β (deg)	110.86(1)	110.74(2)
V (Å^3)	470.84(2)	467.2(1)
Space group	$C2/m$	$C2/m$
2θ-range	3–65	3–60
Indices	±22, ±6, ±14	±21, ±5, ±13
$\sum I$	3908	1829
Unique	1159	780
Observed	1111	754
R_{int} (%)	2.59	5.44
Min./max. tr.	0.0374/0.4109	0.0522/0.5486
N_p	30	30
x	0.0041(1)	0.000 81(4)
w	0.0023	0.000 025
R (%)	2.52	2.66
R_w (%)	2.53	2.84
GOF	1.601	2.326
δF (electrons Å^{-3})	4.42/−5.3	2.46/−4.56

Single-crystal x-ray investigations were performed on a STOE AED II diffractometer, using monochromatized Mo Kα radiation ($\lambda = 0.7107$ Å), equipped with an Oxford cryosystem device. Technical details of the data collection and selected results of the crystal structure refinements are summarized in table 1. A numerical absorption correction was applied for all data sets. The weighting scheme was varied until no significant dependence upon $\sin\Theta/\lambda$ and F_o/F_{max} was observed. The atomic coordinates together with the isotropic displacement parameters are listed in table 2. The interatomic bond lengths are given in table 3.

Table 2. Atomic coordinates and isotropic displacement parameters for $TaTe_2$ at 295 and 120 K.

	x	*y*	*z*	*Ueq*
295 K				
Ta(1)	0	0	0	18(1)
Ta(2)	−1400(1)	5000	−2910(1)	10(1)
Te(1)	57(1)	0	3094(1)	10(1)
Te(2)	−1485(1)	5000	−107(1)	11(1)
Te(3)	−2034(1)	5000	−6229(1)	10(1)
120 K				
Ta(1)	0	0	0	18(1)
Ta(2)	−1397(1)	5000	−2908(1)	10(1)
Te(1)	54(1)	0	3095(1)	10(1)
Te(2)	−1487(1)	5000	−104(1)	11(1)
Te(3)	−2035(1)	5000	−6228(1)	10(1)

Table 3. Selected bond lengths (in Å) for $TaTe_2$ (δ = $(\text{Ta–Te})_{max}$ − $(\text{Ta–Te})_{min}$) at 295 and 120 K.

	295 K	120 K
Ta(1)–Te(1) 2×	2.862(1)	2.857(1)
Ta(1)–Te(2) 4×	2.828(1)	2.824(1)
⟨Ta(1)–Te⟩	2.839	2.835
δ	0.034	0.033
Ta(2)–Te(2)	2.668(1)	2.663(1)
Ta(2)–Te(3)	2.903(1)	2.898(1)
Ta(2)–Te(1) 2×	2.745(1)	2.739(1)
Ta(2)–Te(3) 2×	2.830(1)	2.825(1)
⟨Ta(2)–Te⟩	2.787	2.782
δ	0.235	0.235
Ta(1)–Ta(2)	3.316(1)	3.307(1)
Ta(1)–Ta(1)	3.642(1)	3.631(1)
Ta(2)–Ta(2)	3.642(1)	3.642(1)

Electrical conductivity measurements were performed between 3.5 and 300 K on a single crystal with dimensions $0.1 \times 2 \times 0.1$ mm using a conventional four-probe method. Four gold wires were attached by silver paint yielding a contact resistance below 1 Ω. The temperature was determined by a platinum resistance sensor. The experiments were performed in a helium-flow cryostat with a constant sweep rate of 1–4 min K^{-1}.

3. Band-structure calculations

The electronic band structure of $TaTe_2$ has been calculated charge self-consistently by means of the tight-binding linear muffin-tin orbital (TB-LMTO) method [23] in the ASA mode, including the so-called combined correction terms [24] and using the minimal basis set (the folded down or β-representation) for the wave functions [25]. Accordingly, the dimension of the secular matrix is determined by the number of wave functions with low angular momentum *l* (Ta s, p, d and Te s, p), while wave functions with high angular momentum

Table 4. Parameters and numerical results of the band-structure calculation. The ES are the empty spheres used in the calculations. The Wigner–Seitz radii S_X are given in multiples of the Bohr radius. ΔQ_X represents the charge transfer (total and angular momentum resolved). $n_X(E_F)$ is the density of states at E_F in states Ryd^{-1}/atom, for X = Ta(1), Ta(2), Te(1), Te(2), Te(3), ES(1)–ES(8). The total density of states at E_F, $n_{tot}(E_F)$, is given per formula unit.

		ΔQ_X					
X	S_X	Total	s	p	d	f	$n_X(E_F)$
Ta(1)	3.245	0.283	−1.335	0.883	0.570	0.165	9.983
Ta(2)	2.971	−0.632	−1.461	0.586	0.134	0.107	7.886
Te(1)	3.122	−0.764	−0.271	−0.793	0.218	0.082	3.249
Te(2)	2.963	−1.038	−0.333	−0.953	0.185	0.065	3.088
Te(3)	3.323	−0.243	−0.220	−0.372	0.252	0.097	4.222
ES(1)	2.595	0.594					0.218
ES(2)	2.369	0.525					0.254
ES(3)	1.882	0.302					0.165
ES(4)	1.821	0.377					0.238
ES(5)	1.797	0.272					0.157
ES(6)	1.660	0.170					0.077
ES(7)	1.646	0.354					0.375
ES(8)	1.529	0.238					0.129
$n_{tot}(E_F)$							16.302

(Ta f and Te d, f) contribute to this through the one-centre expansions and the tails of the LMTOs.

As can be seen in table 4, to overcome the open structure of $TaTe_2$, we were forced to introduce eight different types of empty sphere at two Wyckoff sites, in order to fix the upper limit of the overlap between the Wigner–Seitz spheres at 18%. Hence the open crystal structure has been accounted for by the insertion of 15 empty spheres in each unit cell.

Exchange and correlation have been treated within the framework of local density functional theory using the parametrization of Hedin and von Barth. Relativistic effects have been accounted for by using the so-called scalar-relativistic approximation, ignoring the influence of spin–orbit coupling.

The necessary Brillouin zone (BZ) integrations were performed using the tetrahedron method, taking 1272 irreducible $\boldsymbol{k}$-points during the SCF cycle. To get an accurate representation of the Fermi surface, 2807 $\boldsymbol{k}$-points in the irreducible part of the BZ have been used.

4. Results and discussion

4.1. The crystal structure and derived bonding behaviour

As noted in the introduction, the crystal structure of $TaTe_2$ has already been reported, in the 1960s [21]. The lattice parameters given in [21] were $a = 19.31$ Å, $b = 3.651$ Å, $c = 9.37$ Å and $\beta = 134.13^\circ$, which can be transformed to $a = 14.837$ Å, $b = 3.652$ Å, $c = 9.370$ Å and $\beta = 110.91^\circ$. These transformed parameters are in reasonable agreement with the room temperature data given in table 1. Upon cooling, a linear decrease of the unit-cell parameters as well as of the unit-cell volume has been observed (see figure 1). Between

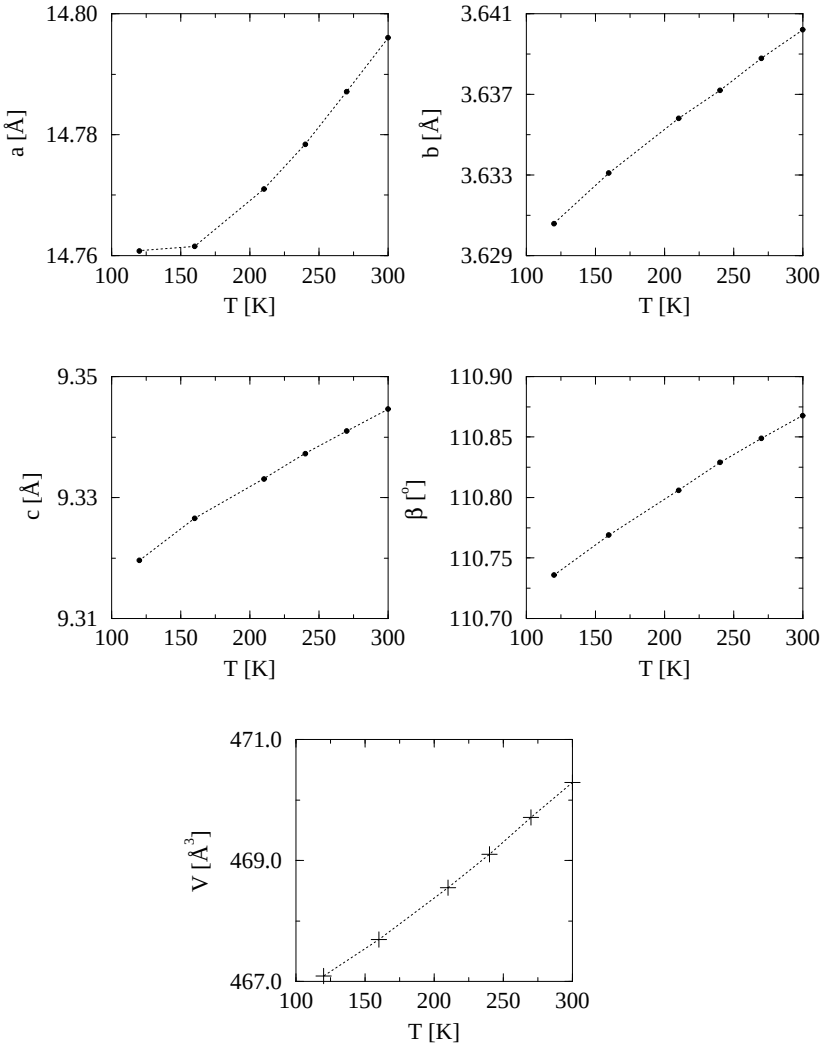

Figure 1. The change of the lattice parameters (top) and of the unit-cell volume (bottom) of $TaTe_2$ upon cooling. (The estimated standard deviations are ±0.002 for the lattice parameters, ±0.03 for the angle and ±0.1 in the case of the volume.)

room temperature and 120 K the unit-cell volume decreases by about 3.6 Å^3 (≈0.8%) and the interatomic bond lengths show a 'normal' decrease with falling temperature, reflecting the rigidity of the material (compare table 3).

The crystal structure of $TaTe_2$ together with the numbering scheme for the various atomic sites are displayed in figure 2 (top). The two Ta centres are in a distorted octahedral environment with Ta–Te distances ranging from 2.828 Å to 2.868 Å for Ta(1) (⟨Ta(1)–Te⟩ = 2.839 Å) and from 2.668 to 2.903 Å for Ta(2) (⟨Ta(2)–Te⟩ = 2.787). It is obvious from these data that the $TaTe_6$ octahedron around Ta(1) is less distorted than that around Ta(2). This is further supported by the δ-parameter, which is defined as the difference $Ta–Te_{max} - Ta–Te_{min}$, having the values 0.034 Å for Ta(1) and 0.235 Å for Ta(2). The Ta–Te bond lengths are within the range reported for other compounds containing $TaTe_6$

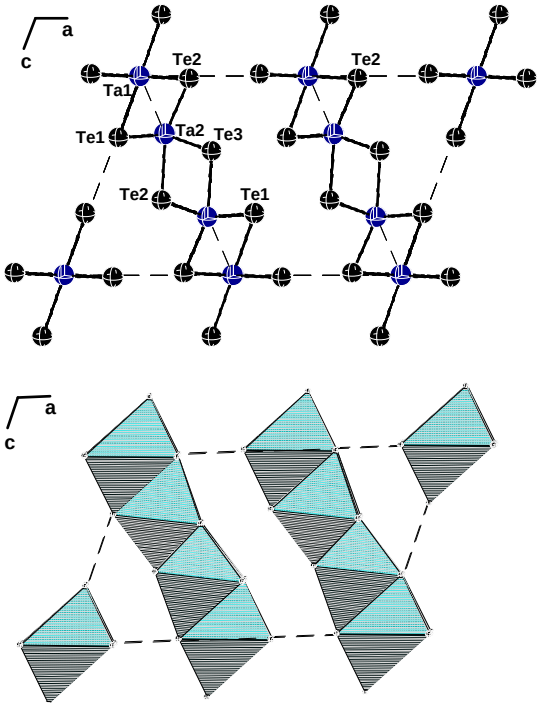

Figure 2. The crystal structure of $TaTe_2$ with the numbering scheme (top) and polyhedral representation of the structure (bottom).

(This figure can be viewed in colour in the electronic version of the article; see http://www.iop.org)

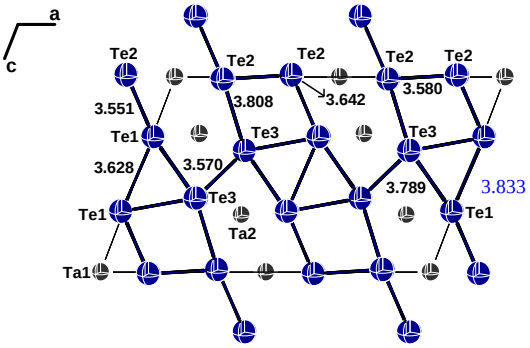

Figure 3. The polymeric Te–Te network in $TaTe_2$.

(This figure can be viewed in colour in the electronic version of the article; see http://www.iop.org)

octahedra ($Ta_3Pd_3Te_{14}$: Ta–Te = 2.644–2.894 Å [22]; $TaTe_4$: 2.807–2.966 Å [26]; $FeTaTe_3$: 2.744–2.875 Å [27]).

The $TaTe_6$ octahedra are joined via common edges, forming slabs running parallel to the [201] direction (see the bottom of figure 2). The shortest intra-slab Te–Te distances amount to 3.551 Å and 3.642 Å, which are significantly shorter than the sum of the van der

Waals radii of Te^{2-} of about 4 Å. The shortest inter-slab contacts are found to be 3.580 Å and 3.642 Å, again distances well within the radius of Te–Te interaction. In addition, there are further Te–Te contacts that are shorter than 4 Å. The resulting 'polymeric' Te network is displayed in figure 3.

In a previous study of the electronic band structure of $TiTe_2$ [2] it was demonstrated that the shortening of the Te–Te distances to 3.77 Å is a consequence of a charge transfer of about 0.38 electrons from Te sp levels to Ti d levels [2]. It was also shown that in the monoclinic modification of VTe_2 the interlayer and intralayer Te–Te distances (range: 3.590 to 3.907 Å for interlayer distances and 3.447 to 3.947 Å for intralayer distances) give rise to a tellurium-to-metal electron transfer of 0.25 electrons per V [2]. A plot of the formal oxidation state per tellurium atom versus Te–Te distances exhibits a linear relationship [6]. Applying this relation also to the Te–Te distances observed in $TaTe_2$, a net charge per tellurium atom of about -1.5 is derived. As a consequence, the formal oxidation state of Ta is $+3$ with a d^2 electronic configuration. For this situation one would expect that the electrons originate from the top of the mostly anionic sp band possessing π-antibonding character.

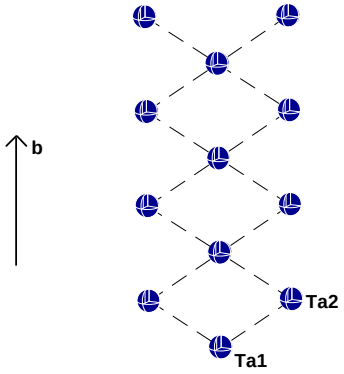

Figure 4. Double-zigzag chains of Ta centres running parallel to the crystallographic *b*-axis in $TaTe_2$.

(This figure can be viewed in colour in the electronic version of the article; see `http://www.iop.org`)

Neglecting this tellurium-to-tantalum charge transfer, Ta should be formally in the oxidation state $+4$, representing a d^1 configuration. It is well documented [2] that such systems are electronically unstable and distortions due to metal-to-metal bond formation are often observed. For a d^1 system a development of metal-atom zigzag chains is expected. But in $TaTe_2$ the metal atoms form double-zigzag chains normally found for d^2 systems (see figure 4). Taking into account the above-mentioned charge transfer, the observed metal-atom network can now be understood qualitatively. The transferred electrons take part in the formation of a net of metal–metal σ-bonds. The Ta–Ta distances within the double-zigzag chains amount to 3.316 (1) Å, which is about 0.4 Å longer than for elemental Ta (2.92 Å).

4.2. Calculated band structures

The atomic valence configurations, $6s^26p^05d^3$ for Ta and $5s^25p^4$ for Te, respectively, with which we started our calculations are used as references for calculating the charge transfer (see the second column in table 4). Obviously, the structural inequivalence of the Ta(1) and

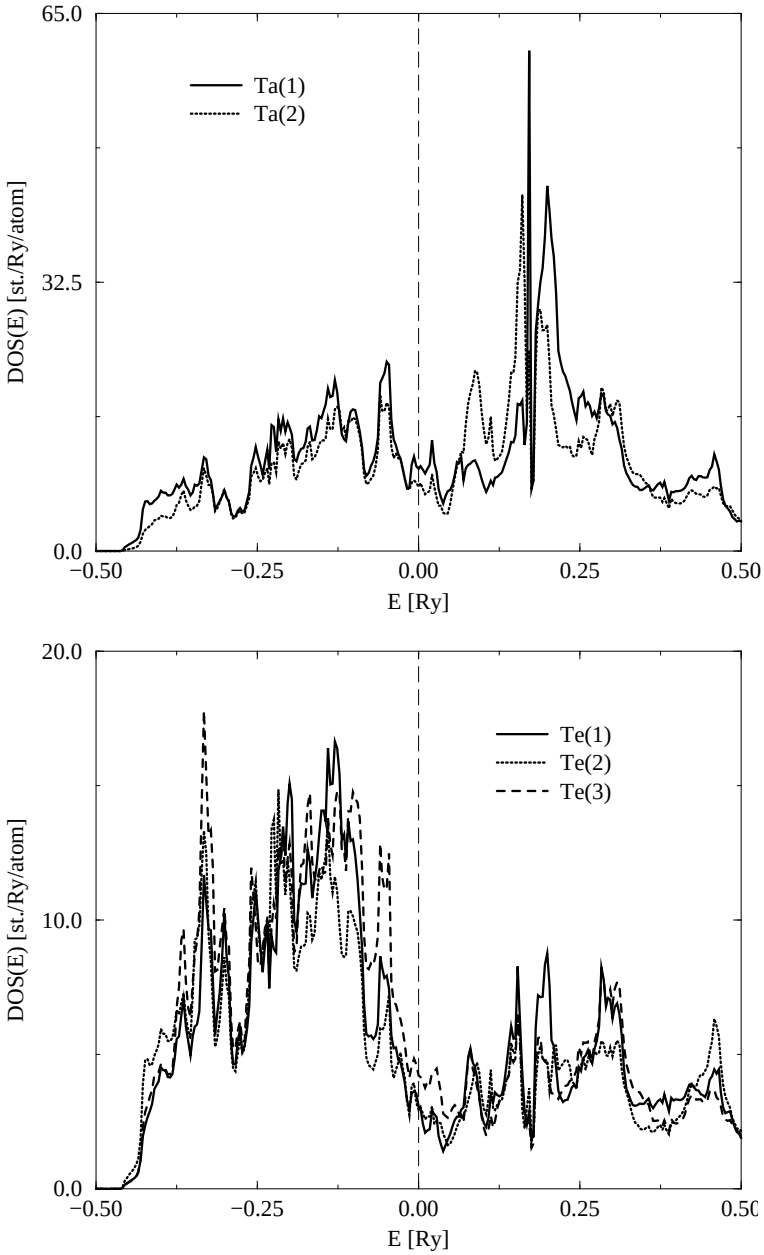

Figure 5. The component-resolved density of states of $TaTe_2$ with the energy given relative to the Fermi level. The top panel gives the contributions of Ta(1) (——) and Ta(2) (· · · · · ·). The lower panel gives the partial densities of states of Te(1) (——), Te(2) (· · · · · ·) and Te(3) (- - - -).

Ta(2) sites is reflected by the transferred charge defined in that way. Because the Wigner–Seitz radius for Ta(1) is nearly 10% larger than for Ta(2), its charge transfer is positive, while that for Ta(2) is strongly negative. The Te atoms, on the other hand, can be seen as reservoirs, supplying the charge to the empty spheres, giving rise to a relatively weak

binding between the $TaTe_6$ octahedra in this way.

These preliminary considerations can be further refined by inspection of the angular-momentum-resolved charge transfer, given in table 4. As one can see, there is a loss of more than one electron in the s channel for both Ta-atom types. In the case of Ta(1) this is more than compensated by a gain in p and d partial charge. For Ta(2), on the other hand, the net charge transfer is negative despite a charge redistribution from s to p and d channels—similar to that found for Ta(1).

The situation for the Te atoms is quite different from that for the Ta atoms. Irrespective of their crystallographic positions, the Te atoms all lose charge from the s as well as the p channel. However, one also notices a small amount of positive charge transfer on the folded down d and f channels. Thus the observed overall trend is quite similar to that found for $TiTe_2$ [2].

The difference between Ta(1) and Ta(2) can also be discussed on the basis of the corresponding partial-density-of-states (DOS) curves. As is shown in figure 5 (top), no qualitative difference occurs in the partial DOSs below the Fermi level, i.e. the partial DOS curve for Ta(2) essentially preserves the shape of the corresponding curve for Ta(1). For that reason the total charge difference can be seen as a consequence of the fact that the former is always somewhat lower than the latter throughout the occupied part of the valence band. For the partial DOS curves, the situation is again quite different for Te. As can be seen in figure 5 (bottom), the gross features of the various inequivalent Te sites are rather similar. Nevertheless, their relative height changes quite rapidly and strongly with the energy, making it impossible to compare the charge transfer for the individual Te sites by means of a simple inspection of the DOS curves alone.

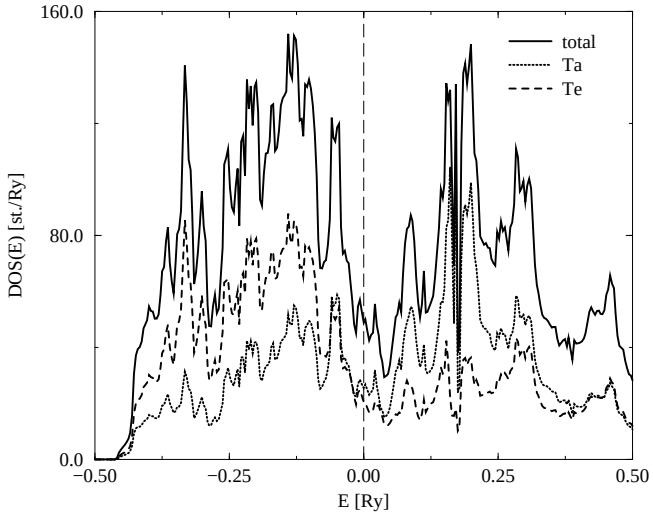

Figure 6. The total (——) and component-resolved density of states relative to the Fermi level. The contributions of the Ta and Te atoms are given by ····· and - - - -, respectively.

The total DOS per unit cell of $TaTe_2$ is shown in figure 6. In addition the component-decomposed parts are given, which are obtained by summing up the contributions from the inequivalent Ta and Te sites (see figure 5). The narrow peak at around 0.8 Ryd below the Fermi level, having mainly Te 5s character, has been omitted from this figure. The position of this peak of course reflects the relatively high binding energy of the atomic Te 5s level

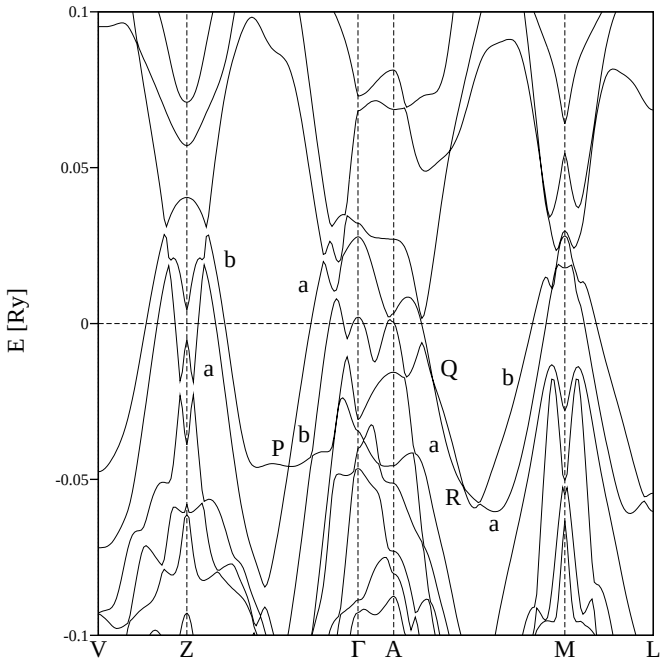

Figure 7. The dispersion relation $E(\boldsymbol{k})$ of $TaTe_2$ for different symmetry lines in the Brillouin zone.

and explains why the s channel of Te as given in table 4 is almost full.

The Te 5s-derived band at around −0.8 Ryd is separated by a gap of 0.33 Ryd width from the valence band shown in figure 6. Inspection of the angular momentum decomposition of the partial DOS curves for the valence band reveals that its Te part is nearly exclusively of 5p character. For Ta, on the other hand, one finds appreciable s and p contributions to the partial DOS. These are primarily located around the lower and upper edge of the displayed region, while they are more or less negligible in the vicinity of the Fermi level. As one would expect from the atomic electronic configuration of Ta and the calculated angular-momentum-resolved partial charges (around 0.6, 0.7 and 3.3 for the s, p and d channels; see table 4), its d contribution dominates the Ta-projected DOS. In particular, the peaks centred at around 0.2 Ryd below and above the Fermi level have primarily d character.

Comparing the partial DOS curves of Ta and Te in figure 6, one finds that, for energies below the Fermi level, the total Te contribution is higher in magnitude than that of Ta, while above the Fermi level the situation is reversed. Accordingly, Ta and Te states contribute to the DOS at the Fermi level to roughly the same extent, with the Ta states slightly dominating (see table 4). Although, as already mentioned, the Ta and Te partial DOS curves differ in their magnitude and variation with energy, one nevertheless notes in figure 6 their very similar structures. This clearly indicates that the two components form common states throughout the whole valence band.

In spite of the rather complex band structure, containing 66 bands for the chosen basis set, there are only two bands cutting the Fermi level, which are labelled a and b in figure 7. According to the previous analysis of the DOS, these bands should originate primarily from the Ta 5d and Te 6p states. This expectation is confirmed by a detailed analysis of the band states. As can be seen in figure 8, both of the bands crossing the Fermi

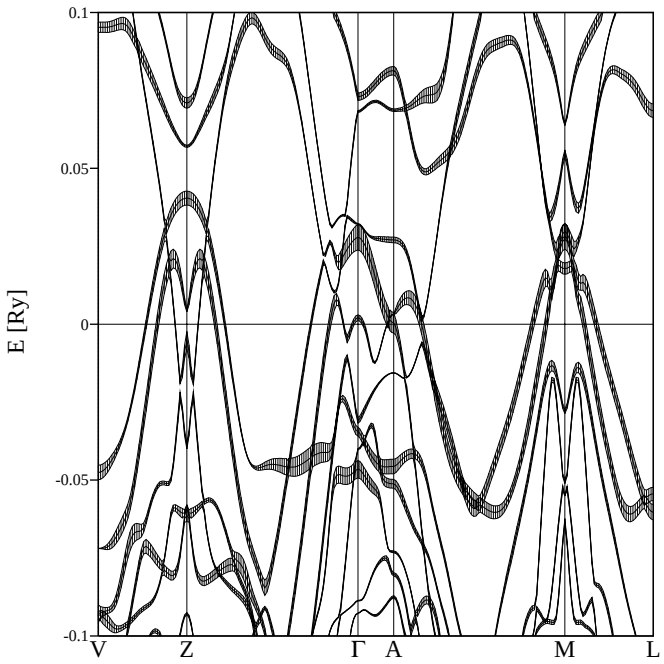

Figure 8. The Ta t_{2g} contribution to the orbital-projected band structure of $TaTe_2$.

level are predominantly of Ta t_{2g} character along most of the directions considered in the BZ (the conventional symmetry symbols t_{2g} and e_g are used here only to group the d orbitals into (d_{xy}, d_{xz}, d_{yz}) and ($d_{3z^2-r^2}$, $d_{x^2-y^2}$), respectively). In addition there is an appreciable contribution of Te p_z character (not shown in figure 8). For the band b along the Γ–A direction, predominantly Ta e_g and Te p_x character is found. This finding is not unexpected because, for the monoclinic structure of $TaTe_2$, the chosen Γ–A direction [28] is not perpendicular to the basal plane V–Z–Γ.

From the above-mentioned analysis, one can conclude that the Ta t_{2g} character results mainly from the hybridization of the Ta(1) d_{yz} and Ta(1) d_{xz} bands with the corresponding bands of Ta(2). The Te p_z character of the bands a and b, on the other hand, stems almost entirely from the Te(3) p_z states. This is in accordance with the calculated charge transfer, and also explains why the p channel of Te(3) is less empty than those of the other Te atoms. The above-mentioned dominating Ta e_g character of band b along the Γ–A direction derives from the hybridization of the Ta(2) $d_{x^2-y^2}$ band with the Te p_x bands.

To get some insight into the phonon-assisted transport mechanisms in $TaTe_2$, such as the electrical conductivity, the Fermi surface which is built up from contributions coming from the bands a and b has been constructed. Figure 9 shows cuts of the Fermi surface with various planes in the reciprocal space. For illustration purposes, the lines and labels of the special $\boldsymbol{k}$-points used in figures 7 and 8 have been added in this figure, together with the corresponding boundaries of the BZ. To distinguish the sheets of the Fermi surface caused by the various bands, those parts of the reciprocal cell for which hole pockets occur have been marked. Proceeding in this manner, the a and b contributions to the Fermi surface can be recognized to supply contours for the various regions shown in the figure. In particular, the white, grey and black areas indicate that two, one or none, respectively, of the bands a and b are below the Fermi level.

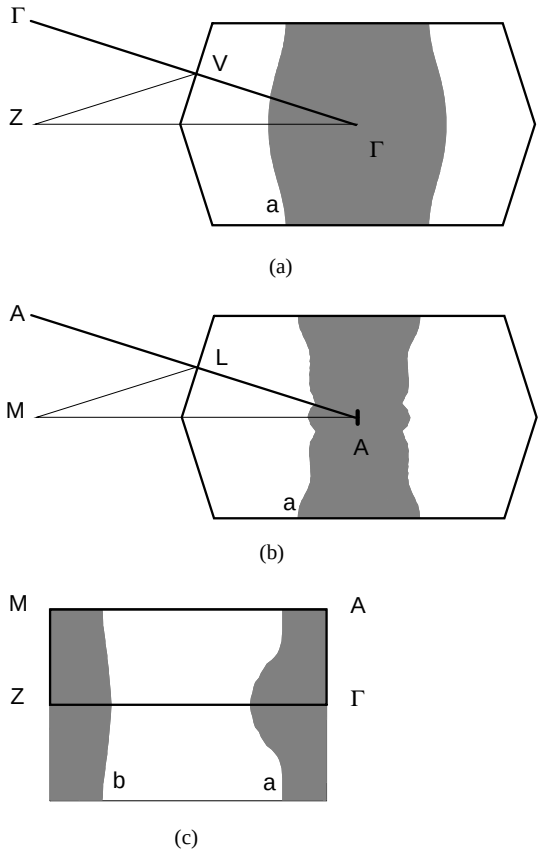

Figure 9. Cuts of the Fermi surface of $TaTe_2$ by the Γ–V–Z (a), A–M–L (b) and Γ–Z–M–A (c) planes. (For more explanation, see the text.)

For the Γ–V–Z plane shown in figure 9 (top) one finds that band a forms the boundary of a large hole pocket centred at Γ, which is open at its top and bottom. Inside this region band b gives rise to several further hole pockets. There is a closed ellipsoid centred at Γ and two small tunnels that are oriented perpendicular to the Γ–V–Z plane. In addition, one notes two relatively large tunnels lying in the Γ–V–Z plane, with their cross section when cut by the Γ–A–M–Z plane shown in figure 9 (bottom). For the A–L–M plane the situation is quite different from that for the Γ–V–Z plane (see the middle of figure 9). There is also a hole pocket centred at A that however is much smaller than that centred at Γ. Furthermore, one notes that the two tunnels perpendicular to the Γ–V–Z plane increased considerably in width and touched the BZ boundary. Finally, one finds four small electron islands.

In conclusion, although the manner in which the phonon-assisted scattering of the electrons on the Fermi surface is classified as a normal (N) or Umklapp (U) process is a matter of definition, one can expect that the presence of large and open holes will raise the probability of U processes as compared to that of N processes.

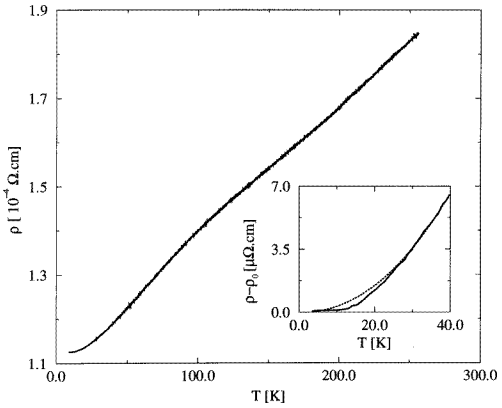

Figure 10. The temperature dependence of the specific resistivity of $TaTe_2$ measured parallel to the crystallographic b-axis. The inset shows a plot of $\rho - \rho_0$ versus T, demonstrating the validity of a power law with the exponent $n = 2.16$ for low temperatures.

4.3. Electrical resistivity

The room temperature specific resistivity of a single crystal of $TaTe_2$ along the b-axis was found to be about 2×10^{-4} Ω cm. The corresponding temperature dependence of the resistivity is displayed in figure 10. On cooling the crystal down to about 3.5 K, the resistivity decreases first in a linear way and exhibits a weak positive curvature starting at about 160 K. The residual resistance ratio, RRR $= R(300\ \mathrm{K})/R(3.5\ \mathrm{K})$, was found to be about 1.6. This can be compared with that for the ternary telluride $TaIrTe_4$, for which a specific resistivity at 300 K of 1.2×10^{-4} Ω cm and a RRR of 1.6 [29] has been found.

According to Matthiessen's rule, the low-temperature dependence of the resistivity of a metal should have the form $\rho = \rho_0 + \rho_1(T)$. The temperature-dependent part ρ_1 can usually be described by $\rho_1(T) = AT^n$ with an exponent ranging from 2 to 5. The validity of such a power law is demonstrated by the inset in figure 10. Below about 40 K the resistivity data follow a power law with $n = 2.16(6)$, reflecting that the scattering giving rise to the resistivity has a predominantly electronic feature. Such small values for the exponent n as about 2 were also reported for low-dimensional metals like $Tl_xV_6S_8$ [30], $In_xV_6S_8$ [31] and $In_xNb_3S_{3.84}$ [32].

5. Summary

We have presented the results of extensive experimental and theoretical investigations of the properties of $TaTe_2$. A very accurate determination of the lattice parameters and atomic positions as well as of their temperature dependence has been performed for this interesting transition metal chalcogen compound. The dominating structural element of $TaTe_2$ is the more or less one-dimensional Ta zigzag chain. The temperature dependence of the measured resistivity has provided evidence that the electron–electron scattering processes are the main cause of resistivity at low temperatures. On the basis of the overall structural properties of $TaTe_2$, a qualitative discussion of its electronic structure and bonding characteristics was given. A more quantitative and detailed description could be supplied on the basis of the band-structure calculations performed. These revealed in particular the interaction of the Ta zigzag chains with the surrounding Te network.

References

[1] Jobic S, Deniard P, Brec R, Rouxel J, Jouanneaux J and Fitch A 1992 *Z. Anorg. Allg. Chem.* **199** 598
[2] Canadell E, Jobic S, Brec R, Rouxel J and Whangbo M H 1992 *J. Solid State Chem.* **99** 189
[3] Rouxel J and Evain M 1994 *Eur. J. Solid State Inorg. Chem.* **31** 683
[4] Van der Lee A, Evain M, Monconduit L, Brec R and Petricek V 1994 *Inorg. Chem.* **33** 3032
[5] Carteaux V, Brunet D, Ouvrard G and Andre G 1995 *J. Phys.: Condens. Matter* **7** 69
[6] Jobic S, Brec R and Rouxel J 1992 *J. Alloys Compounds* **178** 253
[7] Kanatzidis M G 1995 *Angew. Chem.* **107** 2281
[8] Pell M A and Ibers J A 1996 *Chem. Mater.* **8** 1386
[9] Mansuetto M F, Cody J A, Chien S and Ibers J A 1995 *Chem. Mater.* **7** 894
[10] Sheldrick W S and Wachhold M 1996 *Chem. Commun.* 607
[11] Cody J A and Ibers J A 1995 *Inorg. Chem.* **34** 3165
[12] Sheldrick W S and Wachhold M 1995 *Angew. Chem.* **107** 490
[13] Pell M A, Mironov Y V and Ibers J A 1996 *Acta Crystallogr.* C **52** 1331
[14] Bensch W, Helmer O and Näther C 1997 *Mater. Res. Bull.* **32** 305
[15] Bensch W, Heid W, Muhler M, Jobic S, Brec R and Rouxel J 1996 *J. Solid State Chem.* **121** 87
[16] Bensch W, Schur M and Muhler M 1998 in preparation
[17] Meerschaut A, Guemas L, Berger R and Rouxel J 1979 *Acta Crystallogr.* B **35** 1747
[18] Rijnsdorp J, DeLange G J and Wiegers G A 1979 *J. Solid State Chem.* **30** 365
[19] Rijnsdorp J and Jellinek F 1979 *J. Solid State Chem.* **28** 149
[20] Brec R, Grenouilleau P, Evain M and Rouxel J 1983 *Rev. Chem. Miner.* **20** 295
[21] Brown B E 1966 *Acta Crystallogr.* **20** 264
[22] Liimatta E W and Ibers J A 1989 *J. Solid State Chem.* **78** 7
[23] Andersen O K, Jepsen O and Šob M 1987 *Electronic Band Structure and Its Applications (Springer Lecture Notes in Physics 283)* ed M Yussouff (Berlin: Springer) p 1
[24] Andersen O K 1994 *Tight-Binding LMTO, Version 4.6* Max-Planck-Institut für Festkörperforschung, Stuttgart
[25] Lambrecht W R L and Andersen O K 1986 *Phys. Rev.* **34** 2439
[26] Bronsema K D, van Smaalen S, de Boer J L and Wiegers G A 1987 *Acta Crystallogr.* B **43** 3
[27] Liu S X, Cai G L and Huang J L 1993 *Acta Crystallogr.* C **49** 4
[28] Bradley C J and Cracknell A P 1972 *The Mathematical Theory of Symmetry in Solids* (Oxford: Clarendon)
[29] Mar A and Ibers J A 1992 *J. Solid State Chem.* **97** 366
[30] Bensch W, Koy J and Biberacher W 1995 *Solid State Commun.* **93** 261
[31] Bensch W, Koy J and Biberacher W 1995 *Mater. Res. Bull.* **30** 1217
[32] Ohtani T, Sano Y and Yokota Y 1993 *J. Solid State Chem.* **103** 504